

University of Groningen

## **An insight into the extragalactic transient and variable microJy radio sky across multiple decades**

Radcliffe, Jack F.; Beswick, Robert J.; Thomson, A. P.; Garrett, Michael A.; Barthel, Peter D.; Muxlow, Thomas W. B.

*Published in:*  
Monthly Notices of the Royal Astronomical Society

*DOI:*  
[10.1093/mnras/stz2748](https://doi.org/10.1093/mnras/stz2748)

**IMPORTANT NOTE: You are advised to consult the publisher's version (publisher's PDF) if you wish to cite from it. Please check the document version below.**

*Document Version*  
Publisher's PDF, also known as Version of record

*Publication date:*  
2019

[Link to publication in University of Groningen/UMCG research database](#)

### *Citation for published version (APA):*

Radcliffe, J. F., Beswick, R. J., Thomson, A. P., Garrett, M. A., Barthel, P. D., & Muxlow, T. W. B. (2019). An insight into the extragalactic transient and variable microJy radio sky across multiple decades. *Monthly Notices of the Royal Astronomical Society*, 490(3), 4024-4039. <https://doi.org/10.1093/mnras/stz2748>

### **Copyright**

Other than for strictly personal use, it is not permitted to download or to forward/distribute the text or part of it without the consent of the author(s) and/or copyright holder(s), unless the work is under an open content license (like Creative Commons).

The publication may also be distributed here under the terms of Article 25fa of the Dutch Copyright Act, indicated by the "Taverne" license. More information can be found on the University of Groningen website: <https://www.rug.nl/library/open-access/self-archiving-pure/taverne-amendment>.

### **Take-down policy**

If you believe that this document breaches copyright please contact us providing details, and we will remove access to the work immediately and investigate your claim.

Downloaded from the University of Groningen/UMCG research database (Pure): <http://www.rug.nl/research/portal>. For technical reasons the number of authors shown on this cover page is limited to 10 maximum.

# An insight into the extragalactic transient and variable microJy radio sky across multiple decades

Jack F. Radcliffe<sup>1,2,3,4★</sup>, Robert J. Beswick<sup>2★</sup>, A. P. Thomson<sup>2</sup>, Michael A. Garrett<sup>2,5</sup>, Peter D. Barthel<sup>1</sup> and Thomas W. B. Muxlow<sup>2</sup>

<sup>1</sup>Kapteyn Astronomical Institute, University of Groningen, NL-9747 AD Groningen, the Netherlands

<sup>2</sup>Jodrell Bank Centre for Astrophysics, School of Physics and Astronomy, The University of Manchester, Alan Turing Building, Oxford Road, Manchester M13 9PL, UK

<sup>3</sup>ASTRON, the Netherlands Institute for Radio Astronomy, Postbus 2, NL-7990 AA Dwingeloo, the Netherlands

<sup>4</sup>Department of Physics, University of Pretoria, Lynnwood Road, Hatfield, Pretoria 0083, South Africa

<sup>5</sup>Leiden Observatory, Leiden University, PO Box 9513, NL-2300 RA Leiden, the Netherlands

Accepted 2019 September 27. Received 2019 September 25; in original form 2019 February 22

## ABSTRACT

The mJy variable extragalactic radio sky is known to be broadly non-changing with approximately 3 per cent of persistent radio sources exhibiting variability that is largely active galactic nucleus-related (AGN). In the faint ( $< \text{mJy}$ ) flux density regime, it is widely accepted that the radio source population begins to change from AGN dominated to star formation dominated, together with an emergent radio-quiet AGN component. Very little is known about the variable source component in this sub-mJy regime. In this paper, we provide the first insight into the  $\mu\text{Jy}$  variable sky by performing a careful analysis using the deep VLA data in the well-studied GOODS-N field. Using five epochs spread across 22 yr, we investigate approximately 480 radio sources finding 10 that show signs of variability. We attribute this variability to the presence of an AGN in these systems. We confirm and extend the results of previous surveys, finding that variability in the faint radio sky is rather modest with only  $\leq 2$  per cent of sources exhibiting significant variability between any two epochs. We find that 70 per cent of variable sources show variability on time-scales of a few days while on longer decadal time-scales, the fraction of variable sources decreases to  $< 1$  per cent. This suggests that the radio variability peaks on shorter time-scales as suggested by other studies. We find that 80 per cent of variable sources have VLBI counterparts, and we use multiwavelength data to infer that these may well be core-dominated FR-I sources as postulated by the wide-field VLBI surveys and semi-empirical simulations.

**Key words:** techniques: interferometric – galaxies: active – radio continuum: transients.

## 1 INTRODUCTION

Extremely deep radio observations of extragalactic fields have now revealed the nature of the persistent sub-100  $\mu\text{Jy}$  radio source population. It is generally agreed that at  $\mu\text{Jy}$  flux densities the radio source population is dominated by moderate to high-redshift star-forming galaxies and radio-quiet active galactic nuclei (AGNs). This is in contrast to the radio source counts at flux densities of  $\sim \text{mJy}$  and above, which are dominated by radio galaxies and quasars (e.g. Muxlow et al. 2005; Padovani et al. 2015; Smolčić et al. 2017, and references therein).

While deep field studies are providing a view of the  $\mu\text{Jy}$  radio sky in the spatial and spectral domains, at present comparatively little is known about their intrinsic variability in this faint flux density regime. Previous studies have shown that the variable and transient radio sky consists of a range of interesting astrophysical phenomena. Within our own Galaxy, these can range from flaring stars and X-ray binaries (e.g. Thyagarajan et al. 2011; Williams et al. 2013) to novae and pulsars (e.g. Healy et al. 2017), while the transient and variable extragalactic radio sky includes AGNs, tidal disruption events, supernovae, gamma-ray bursts, fast radio bursts, and the recently observed binary neutron star mergers (e.g. Berger et al. 2003; Lorimer et al. 2007; Fong et al. 2014; Hallinan et al. 2017). Of the slower transients (on time-scales of minutes or longer), AGNs are by far the most common extragalactic radio variable sources ( $\gtrsim 60$  per deg<sup>2</sup> above 0.3 mJy) and are found to

\* E-mail: jack.radcliffe@manchester.ac.uk (JFR);  
robert.beswick@manchester.ac.uk (RJB)

vary at all frequencies on time-scales from minutes to years (e.g. Dennett-Thorpe & de Bruyn 2002; Lovell et al. 2008; Ofek et al. 2011; Hodge et al. 2013; Mooley et al. 2013; Pietka, Fender & Keane 2015; Mooley et al. 2016).

Many transient surveys are focused on relatively short-duration events, such as radio afterglows of gamma-ray bursts, however there have been few studies on the slowly varying radio sky. From the few longer term variability surveys that exist, the faint ( $> 0.5$  mJy) radio sky appears to be broadly non-variable, with only  $\sim 3.6$  per cent of sources showing variations over week to 1.5 yr time-scales (Mooley et al. 2016). Over still longer time-scales (7–20 yr), it was found that only  $\sim 1$  per cent of extragalactic sources in the mJy regime (excluding galactic transients) are variable (Becker et al. 2010; Croft et al. 2010; Bannister et al. 2011b).

However, these previous studies have a number of limitations. Long-term (several years) variability surveys are reliant on archival data such as the FIRST/NVSS survey with limited sensitivity ( $1\sigma$ , 0.2 mJy) and thus are only able to probe the brighter end of the transient radio luminosity function. The next generation of radio interferometers, such as the Karl G. Jansky Array (JVLA; Perley et al. 2011), e-MERLIN, ASKAP (Johnston et al. 2008), LOFAR (van Haarlem et al. 2013), MeerKAT (Booth et al. 2009), Apertif/WSRT (Oosterloo, Verheijen & van Cappellen 2010), the Square Kilometer Array (SKA; Dewdney et al. 2009), and the next-generation VLA (e.g. Carilli et al. 2015), with their much improved survey speeds and snapshot sensitivity will be able to study the faint transient radio population across large areas of the sky.

The GOODS-N field has had multiple  $\mu$ Jy sensitivity observations at 1.4 GHz spanning over 22 yr using both the Very Large Array (VLA; Richards 2000; Biggs & Ivison 2006; Morrison et al. 2010) and the recently upgraded JVLA (Owen 2018, Radcliffe et al. in preparation) with cadence times from a few days to decades.<sup>1</sup> In this paper, our goal is to use this unique data set to investigate the  $\mu$ Jy variable sky over a 22 yr period, probing the variable properties of over 400 hundred faint extragalactic sources.

This paper is organized as follows. In Section 2, we present the observations, data reduction, and imaging. We outline the steps used to define our variable sample in Section 3 and our results are presented in Section 4. We discuss the implications of our results and compare to other variability surveys in Section 5. Concluding remarks are given in Section 6.

Throughout this paper, we adopt a spatially flat six-parameter  $\Lambda$ CDM cosmology with  $H_0 = 67.8 \pm 0.9$  km s<sup>-1</sup> Mpc,  $\Omega_m = 0.308 \pm 0.012$ , and  $\Omega_\Lambda = 0.692 \pm 0.012$  (Planck Collaboration XIII 2016). For spectral index measurements, we use the convention  $S_\nu \propto \nu^\alpha$  throughout, where  $S_\nu$  is the radio integrated flux density and  $\alpha$  is the intrinsic source spectral index.

## 2 DATA

### 2.1 VLA observations

In 1996 November, a total of 50 h of VLA (A-configuration; VLA project code AR0368) 1.4 GHz observations, centred within the GOODS-North region at J2000 RA 12<sup>h</sup>36<sup>m</sup>49<sup>s</sup>.4 DEC +62°12'58"0 were observed in a pseudo-continuum, spectral line mode. This was divided into two frequency sub-bands or spectral windows (spw),

with central frequencies of 1.365 and 1.435 GHz and a combined total bandwidth of 43.75 MHz. Each spectral window comprised of  $7 \times 3.125$  MHz wide channels. For the purpose of this study, we have reanalysed these data using modern absolute flux scales and advanced calibration techniques that were not available at the time of the original publication of Richards (2000).

The source J1313+6735 ( $S_{1.4\text{GHz}} = 2.4$  Jy) was used as an amplitude, phase, and bandpass calibrator and was observed every 40 min. 3C 286 was used as the flux density calibrator where the assumed flux densities of 15.328 and 14.947 Jy at 1.385 and 1.435 GHz, respectively, are derived from the Perley & Butler (2017) absolute flux density scale. We discuss how differing flux scales between various observations are a vital consideration for any variability study in Section 3.4.

All calibration was conducted using the Common Astronomy Software Applications (CASA; McMullin et al. 2007). The raw VLA data sets for the entire 50 h were imported into a single  $uv$  measurement set using IMPORTVLA. Due to known issues with the old VLA MODCOMP control computers, the task FIXVIS was used to correctly recalculate the  $u$ ,  $v$ , and  $w$  visibility coordinates. These data were then inspected and radio frequency interference (RFI) was removed using a combination of CASA tasks FLAGDATA, VIEWER and PLOTMS along with the RFUI viewer packaged with the AOFLAGGER software (Offringa, van de Gronde & Roerdink 2012). Once the strongest RFI was excised, a gain curve, describing the forward gain of each antenna, was derived using GENCAL. The absolute flux scale was set using an  $L$ -band model of 3C 286 using SETJY (Perley & Butler 2017). Bandpass calibration was conducted on a per scan basis using calibrator, J1313+6735, and a complex gain calibration (amplitude and phase) was conducted on J1313+6735 and 3C 286 with 5 min averaging interval using GAINCAL. This calibration table was used to bootstrap the flux density scale from 3C 286 to J1313+6735. The integrated flux density of J1313+675 was found to be 2.396 Jy at 1.40 GHz, which is within 0.2 per cent of the quoted value of 2.40 Jy.<sup>2</sup>

These calibration solutions were applied to the GOODS-N target field, which was split from the original data set. The data were reweighed to obtain the ideal sensitivity (using STATWT), and any remaining RFI was excised from the data. Confusing sources were removed from the data following the procedures outlined in Section 2.3 and then self-calibration was performed on the target field (calibrating each polarization separately) using multiple target sources, contained within a central 10 arcmin diameter area, as a model. Due to the complexity of the sky model, self-calibration used an iterative strategy with solution intervals beginning at 20 min and culminating with 2 min solution intervals for the final self-calibration cycle. No amplitude self-calibration was conducted.

### 2.2 JVLA observations

The JVLA (A-configuration) observed the GOODS-N field for a total of 38 h in between 2011 August and September (VLA project code TLOW0001; PI: F. Owen) and a further 10 h in 2018 May (VLA project code 18A-392; PI: J. Radcliffe). For the purposes of this study, we only use 20 h of the JVLA2011 data, which provides two epochs with similar observing times (see Table 1). The observations have a total bandwidth of 1024 MHz comprising 16 spw with 64 channels per spw.

<sup>1</sup>Note that in this paper, we use observations from before and after the VLA electronics upgrade, hence the term JVLA will correspond to post-upgrade and the term VLA to pre-upgrade.

<sup>2</sup><https://science.nrao.edu/facilities/vla/observing/callist>



**Table 1.** A summary of the individual VLA/JVLA epochs utilized in this paper. The epochs correspond to the data that are compared on long time-scales, typically 7–22 yr whereas sub-epochs are those data used to establish any short-term variability typically within a few days. This epoch and sub-epoch naming conventions used here are adopted throughout the paper. Note that the VLA observations were comprised of 24 observations spread over 1 month where the total observing time was approximately 47 h on source.

Telescope	VLA project code	Epoch	Sub-epoch	Date (UT)	Frequency (GHz)	Rms ( $\mu\text{Jy beam}^{-1}$ )
VLA	AR0368	VLA1996	–	1996 Nov 1–1996 Dec 1	1.35–1.45	5.6
JVLA	TLOW0001	JVLA2011	JVLA2011 ep1	2011 Sep 9; 12:57:47–17:56:57	1.00–2.03	2.80
–	–	–	–	2011 Sep 9; 18:00:25–22:59:35	–	–
–	–	–	JVLA2011 ep2	2011 Sep 11; 11:49:53–15:49:01	–	–
–	–	–	–	2011 Sep 11; 15:49:11–20:48:20	–	–
–	–	–	–	2011 Sep 11–12; 20:48:26–01:47:36	–	–
JVLA	18A-392	JVLA2018	JVLA2018 ep1	2018 May 9; 06:27:27–08:25:28	1.00–2.03	3.98
–	–	–	–	2018 May 12; 06:21:33–08:19:39	–	–
–	–	–	JVLA2018 ep2	2018 May 15; 03:24:20–05:22:26	–	–
–	–	–	–	2018 May 16; 01:14:41–03:12:43	–	–
–	–	–	–	2018 May 19; 01:23:49–03:34:10	–	–

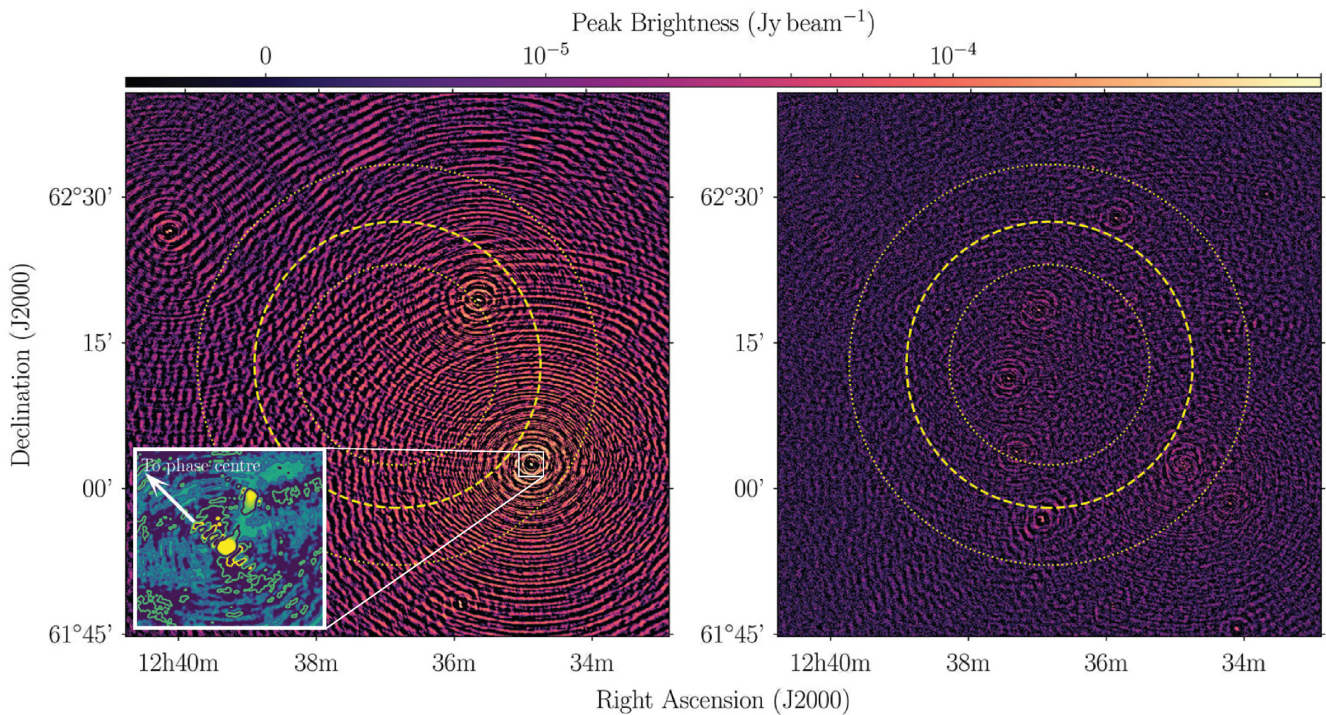


**Figure 1.**  $1^\circ \times 1^\circ$  image of the 1996 VLA data illustrating the source removal routine used outlined in Section 2.3. The yellow dashed circle corresponds to the HPBW of a VLA antenna at 1.4 GHz ( $\sim 29''.5$ ) while the dotted circles correspond to the VLA HPBW at 1 and 2 GHz ( $\sim 41''.2$  and  $\sim 20''.6$ , respectively). The symmetric logarithmic colour scale is the same for both the panels and ranges from  $-5 \mu\text{Jy beam}^{-1}$  to  $0.8 \text{ mJy beam}^{-1}$ . *Left-hand panel:* The data before the source removal process. Ripples from off-axis sources severely affect the central target field. The inset is a cut-out of S1 (J2000 12h35m38.044s + 62d19m32.097s) illustrating the un-deconvolvable side lobes present in the 1996 VLA data, which are directed towards the phase centre. *Right-hand panel:* The data post the removal of confusing sources revealing sources located in the centre of the field.

The source J1313+6735 was used as a phase and bandpass calibrator and 3C 286 was used as the flux calibrator. Initial flagging was conducted using AOFLAGGER (Offringa et al. 2012). The VLA CASA pipeline<sup>3</sup> was then used to conduct the flux density scaling and phase referencing. Some epochs required additional flagging (and re-calibration) after the initial pipeline calibration, especially if strong RFI had not been flagged adequately before or during

calibration. In total, approximately 20–40 per cent of the data in each epoch were lost due to RFI.

### 2.3 Off-axis source removal

As has been noted in previous publications dealing with the GOODS-N field, there are significant issues with bright, confusing sources that limit the dynamic range of the central image. In order to deal with these sources, we were required to remove a number of sources from these data. Confusing sources were identified by

<sup>3</sup><https://science.nrao.edu/facilities/vla/data-processing/pipeline>

generating a large,  $2^\circ \times 2^\circ$ , un-deconvolved image using WSCLEAN (Offringa et al. 2014).

The influence of off-axis confusing sources was more severe in the old VLA observations. The pre-WIDAR, VLA correlator had significant multiplicative off-axis errors when the continuum mode was used. These errors are correlated with the visibility strength resulting in un-deconvolvable side lobes around the brightest sources that are orientated towards the phase centre (see the inset in Fig. 1). This has been previously noted by Richards (2000), Biggs & Ivison (2006), and Morrison et al. (2010). As a result, sources as far as  $2^\circ$  from the phase centre had to be carefully subtracted. For the JVLA data, these errors have been fixed with the upgrade to the WIDAR correlator. As a result, fewer sources needed to be peeled and the main source of confusion was due to the primary beam attenuation inducing direction-dependent errors upon bright sources near the primary beam half-power.

With confusing sources identified, each was removed individually using the following procedure:

(i) A frequency-dependent model of the source was generated using CASA task TCLEAN and the multi-term multi-frequency synthesis (MT-MFS) algorithm (Rau & Cornwell 2011). Separate models were generated for each of the circular polarizations due of the significant beam squint of the VLA antennas.

(ii) The model generated was then Fourier transformed and gridded in order to generate model visibilities (using task FT).

(iii) Calibration corrections, derived by comparing the observed visibilities to the model visibilities and solving per antenna, were generated using GAINCAL. The observed visibilities were adjusted by these corrections using task APPLYCAL.

(iv) Steps (i)–(iii) were repeated until the side-lobe structure around the confusing source was reduced.

(v) The final self-calibration model visibilities were subtracted from the observed visibilities using task UVSUB. This removed the source and the side-lobe structure from the observed visibilities.

(vi) The observed visibilities now have the correct phase and amplitude solutions at the location of the confusing source rather than the pointing centre. Therefore, we must revert our complex gains to the centre of the target field. To do this, the amplitude and phase corrections contained in final calibration table were inverted using the contributed CASA task INVGAIN (Hales 2016).

(vii) These inverted corrections were applied (using task APPLYCAL) to adjust the observed visibilities to be correct for the point centre again.

(viii) Finally, steps (i)–(vii) were repeated for the other confusing sources.

The results of this process are presented in Fig. 1. This removal method is identical to the ‘peeling’ method commonly used in radio interferometric data processing (e.g. Owen & Morrison 2008; Intema et al. 2009) with the exception that we do not reinsert the self-calibrated source model into the visibilities after step (viii). This meant that we were not required to deconvolve these sources when generating the final images, thus reducing the image size required.

## 2.4 Imaging

A large  $35 \text{ arcmin} \times 35 \text{ arcmin}$  image was generated for each data set using CASA task TCLEAN. Imaging for both the JVLA and VLA used the WPROJECTFT algorithm (Cornwell, Golap & Bhatnagar 2008). This algorithm accounts for the non-coplanar array term (known as the  $w$  term), thus minimizing the induced smearing away from the phase centre. For these VLA data, deconvolution

was performed using the CLARKSTOKES algorithm. A primary beam model for the VLA correction was derived using the CASA recipe MAKEPB and then was divided through the image using IMPBCOR.

For these JVLA data, the imaging method was slightly different. Due to the large fractional bandwidth ( $\sim 68$  per cent), deconvolution was performed using the MT-MFS technique, which permits more accurate deconvolution by taking into account the frequency dependence of the sky model (Rau & Cornwell 2011). In addition, this method allows the correction of the difference in reference frequencies<sup>4</sup> utilizing the in-band spectral indices to correct fluxes to that of the same frequency as the VLA data. This technique is tested and outlined in Section 3.3. The images were corrected for the primary beam attenuation and primary beam-induced spectral curvature using the WIDEBANDPBCOR CASA task. The final data sets, epochs, and sensitivities of the various epochs are described in Table 1.

## 3 DEFINING A VARIABLE SAMPLE

With the images generated, we can now proceed on to the variability analysis. This section aims to summarize our selection method for defining the variable population while outlining and addressing the various systematic offsets that could induce artificial variability between the various epochs. These effects include the source-extraction software, the reference frequency, the differing  $uv$  coverage, and the absolute flux scale. We shall address in turn each of these issues. Because we expect from previous studies that the number of variable sources will be low, systematics that can affect individual source flux densities (e.g. source extraction) are much more important to address than those that affect the source flux densities as a whole (e.g. absolute flux density scaling) as these can be modelled and corrected.

### 3.1 Source extraction

One of the most important systematics to address is the varying performance of the chosen source-extraction routine. There are two main effects to consider, the first being the false detection rate and the second being the recovered flux densities of the extraction software. To identify sources, we will use PYBDSF (Mohan & Rafferty 2015).

#### 3.1.1 False detection fraction

In order to determine the appropriate signal-to-noise (S/N) threshold at which to allow PYBDSF to identify and catalogue sources in our maps, we adopt the empirical ‘purity’ parameter of Stach et al. (2018). We ran PYBDSF on the real and inverted images (i.e. the real maps multiplied by  $-1$ ) for each epoch with S/N thresholds between 3 and 8, and we then evaluated the ‘purity parameter’,

$$P_r = \frac{N_p - N_n}{N_p}, \quad (1)$$

for each image, where  $N_p$  is the number of sources detected above a given S/N limit in the real image and  $N_n$  is the number of sources detected above the same S/N limit in the inverted image. For an idealized image comprising Gaussian noise and a real source

<sup>4</sup>The reference frequency is the centre of the band and, when using MT-MFS, is where the wide-band image flux density should equal the source flux density (see Section 3.3).

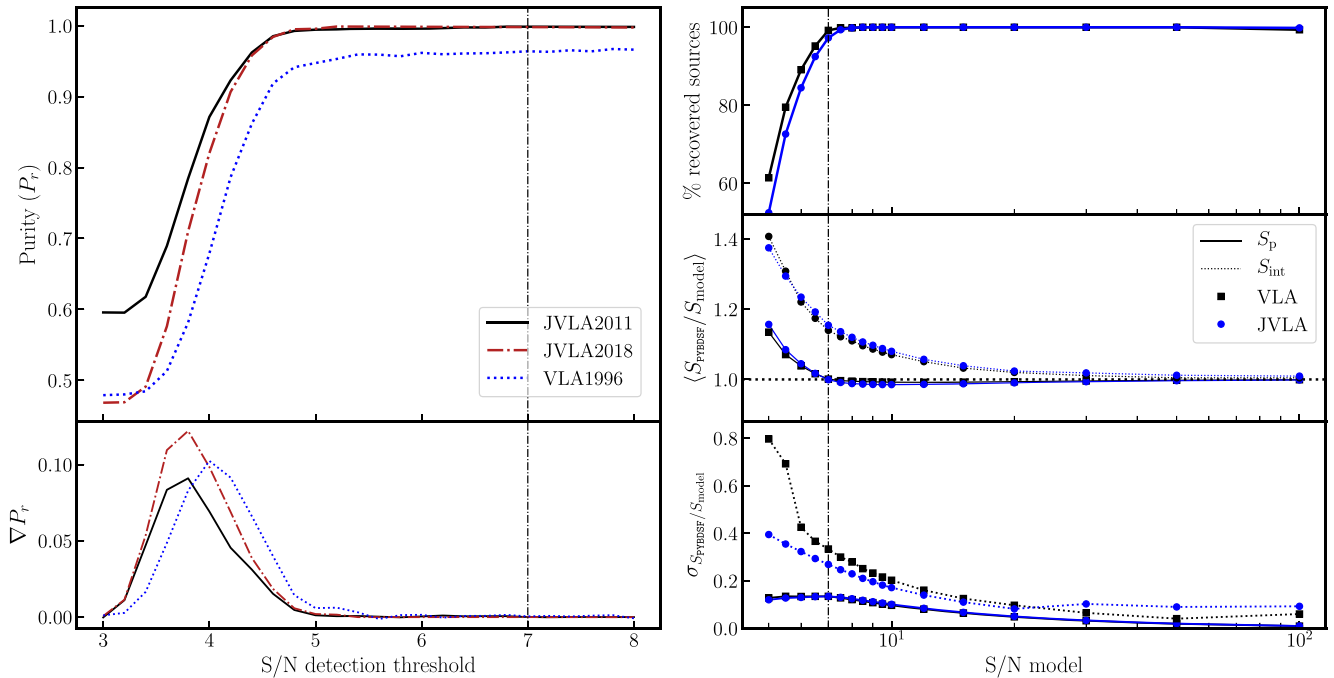


**Figure 2.** Summary of the various source-extraction tests performed using PYBDSF. *Left-hand panel:* The purity,  $P_r$  parameter against S/N detection threshold. The number of false detections in all epochs ( $> 3$  per cent) is large at  $S/N < 5$ . The parameter asymptotes for all epochs at around S/N thresholds of 5.5 as illustrated by the gradient of the purity parameter,  $\nabla P_r$ , in the bottom panel. *Right-hand panel:* The results from the flux recovery simulations using PYBDSF. The top panel illustrates the percentage of model sources recovered by the source-extractions software. The middle panel shows the average flux recovery performance while the bottom panel shows the typical  $1\sigma$  variance on the average recovered flux densities. The  $7\sigma$  detection threshold adopted in these analyses provides good peak brightness recovery with a typical error of around 12 per cent and recovers the majority of sources inserted  $\sim 98$  per cent.

population, at an arbitrarily high S/N threshold the purity parameter should asymptote towards unity (i.e.  $N_p > 0$  and  $N_n = 0$ ). However, at lower S/N thresholds, we expect to detect a combination of genuine sources and spurious noise peaks in the real image, and only spurious noise peaks in the inverted image.

As Fig. 2 illustrates, the purity parameter asymptotes towards unity around an S/N threshold of 5 for epochs observed with JvLA, whereas for the pre-upgrade VLA maps the purity parameter asymptotes to  $\sim 0.97$ . We determine that the VLA false-positive rate asymptotes to  $\sim 3$  per cent for  $S/N \gtrsim 5.5$ . This is indicative of non-Gaussian noise properties in the VLA maps due to a combination of multiplicative baseline errors (which cause visible corrugations in the maps towards the pointing centre), and the more limited  $uv$  coverage of the old array with respect to the post-2010 JvLA. Visual inspection of the inverted maps confirms this, and these highly localized areas are excluded during subsequent cataloguing.

### 3.1.2 Flux recovery

In addition to ensuring that the S/N threshold reduces the number of false positives to a minimum, for variability studies, we also have to evaluate the source-extraction technique and any systematic biases to the recovered flux densities. One of these biases is the well-noted ‘flux-boosting’ effect (Jauncey 1968; Vernstrom et al. 2016). This causes the fitted flux densities, especially in the low-S/N regime, to be systematically overestimated due to a combination of confusion and instrumental noise. For deep radio surveys, this manifests itself as an overestimation of the faint source counts. In the case of variability studies, this effect can be significant if the sources between the two epochs being compared have differing S/N

ratios. The flux boosting effect is a function of S/N, therefore a source will be flux boosted in the less sensitive image resulting in artificial variability between epochs. The severity of this effect is also related to the choice of the source-extraction routine.

In these tests, we performed a hybrid approach that uses real observations (including residual calibration errors) with simulated sources injected. This was done separately for the VLA and JvLA due to the differing  $uv$  coverage and therefore different noise characteristics. Before simulated sources were injected, a sky model was generated using WSCLEAN, utilizing the automasking routine to ensure that only real sources are removed and the noise characteristics are not changed. This model is Fourier transformed and subtracted from the visibilities and then the  $uv$  data are imaged again to generate blank  $7k \times 7k$  pixel noise fields. These images are used to generate an r.m.s. map using PYBDSF.

These model sources comprise simple delta functions with a range of S/N ratios. These are convolved with the restoring beam and added into the noise fields. The positions of these sources are randomized across the field of view with the restriction that a source cannot be 10 pixels from another source in order to prevent blending complications. In addition, the periphery of the image ( $\sim 10$  per cent of the total image size) is avoided in order to reduce complications due to CLEAN aliasing. Each image is then catalogued using PYBDSF using a  $5.5\sigma$  detection threshold (as motivated by the purity tests).

The results of these simulations are summarized in Fig. 2. The peak brightnesses of the simulated sources are generally recovered by PYBDSF at around an S/N of 7. Below this threshold, the detected source flux distribution is censored where some sources that have their flux densities reduced by natural noise fluctuations are not



detected. As a result, we see the flux-boosting effect that increases the average recovered flux densities in the low-S/N regime. It is worth noting here that at intermediate-S/N ratios ( $S/N = 10\text{--}40$ ) the peak brightnesses are, on average, underestimated by  $\sim 1$  per cent. While only small, this effect occurs due to the overestimation of the source size, which reduces the fitted peak brightness while increasing the integrated flux densities. This is illustrated by the integrated flux densities being, on average, 5–10 per cent larger than the peak brightnesses in this S/N regime. In light of these conclusions, we adopt a conservative S/N threshold of  $7\sigma$  for our detection threshold, which provides a high reliability (as shown by the purity and sources recovered metrics) and adequate peak flux recovery (albeit with  $\sim 12$  per cent errors) in this S/N regime.

### 3.2 $uv$ coverage

One potential source of induced variability could be caused by the differing  $uv$  coverage of the various epochs. The multifrequency synthesis imaging approach improves the sensitivity and fidelity of interferometric images by utilizing the large bandwidths to fill the  $uv$  plane. The large differences between the bandwidths of the VLA and JVLA observations therefore cause a mismatch in the  $uv$  coverage. This effect is more significant on complex structures with differing radio power on multiple spatial scales; however, the majority of the radio sources in this field are not extended and subtend only 1–2 VLA beam widths. To address this issue, we excluded large extended sources (with classical radio jet structures) by masking them before cataloguing, and we did not consider those sources that required models comprising multiple Gaussian components by PYBDSF in order to model their flux distribution. In addition, we only consider the peak brightnesses of sources as these radio emission mechanisms will have the same power on all spatial scales and are thus less sensitive to differences in the  $uv$  coverage. It is worth noting that these cuts will inevitably bias our result as we may miss variable sources associated with extended objects. However, such variability would be difficult to disentangle from artificial variability induced by the differing  $uv$  coverage between the epochs.

### 3.3 Reference frequency

The reference frequency is the frequency in which the wide-band flux densities in interferometric images equal the narrow-band flux densities. This frequency  $\nu_{\text{ref}}$  is simply defined as the centre of the observing band,

$$\nu_{\text{ref}} = \frac{\nu_{\text{high}} - \nu_{\text{low}}}{2}, \quad (2)$$

where  $\nu_{\text{low}}$  and  $\nu_{\text{high}}$  correspond to the low and high edges of the observing bandwidth, respectively.<sup>5</sup> The intensity of an image is such that the wide-band flux density is equal to the narrow-band source flux density at the reference frequency. Without taking into account the frequency dependence of the sky brightness distribution, this intensity is simply the weighted mean of the flux density across the bandwidth. This makes the returned fluxes susceptible to bias from the flagging of large frequency ranges. However, if MT-MFS is used, the flux densities are fitted across the band and so the returned wide-band flux density will be closer to the real narrow-band flux density (Emonts private communication). This makes the returned flux densities more robust to any flagged data.

<sup>5</sup>See <https://casa.nrao.edu/casadocs/casa-5.6.0/imaging/synthesis-imaging/wide-band-imaging> for more information.

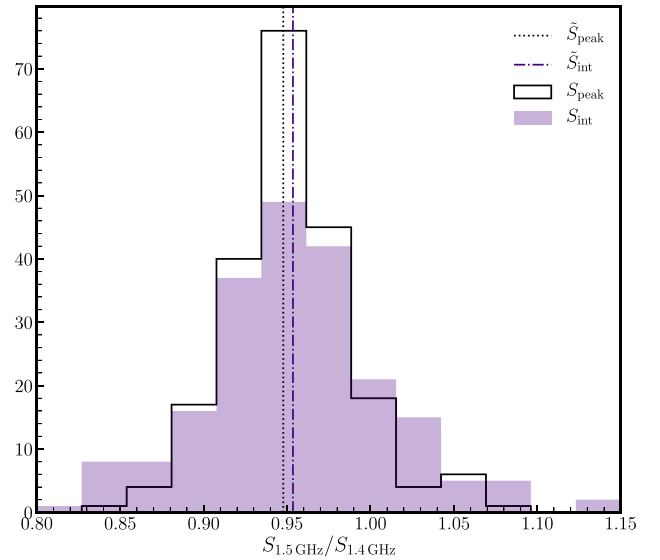


**Figure 3.** Comparison between the 1.4 and 1.52 GHz fluxes of the JVLA data of epoch 5 (observed in 2018). The indigo filled and black edged histograms correspond to the ratio of peak brightnesses and integrated flux densities, respectively. The corresponding dashed lines indicate the median of each distribution. The large scatter of both distributions is dominated by the intrinsic scatter in the individual source spectral indices.

One possible source of induced variability is the differing reference frequencies between the VLA (1.4 GHz) and JVLA (1.52 GHz) epochs. Over the entire radio source sample, the differences between the two reference frequencies will manifest as a systematic flux scaling issue around the median spectral index of the source population. Indeed, Owen (2018) finds an  $\sim 6$  per cent systematic flux density decrease between the JVLA data used in these analyses and the Morrison et al. (2010) VLA observations, which is consistent with the difference in flux density expected between 1.4 and 1.52 GHz with a mean spectral index in the expected range of  $(-0.7)\text{--}(-0.8)$ . While the net effect of this can be fitted and removed, the large intrinsic scatter in the spectral index distribution ( $\alpha = -0.73 \pm 0.35$ , Smolčić et al. 2017) means that a small fraction of sources with extreme deviations could significantly change the flux densities between 1.4 and 1.52 GHz.

For studies of the entire population as a whole, this is not significant, but in the case of variability where we expect a small number of variable sources, this effect could be significant on the final variable population identified. To correct for this, we utilize the MT-MFS algorithm when imaging the JVLA epochs to adjust the reference frequency to 1.4 GHz. This algorithm uses the in-band source spectral index to rescale each source to the appropriate flux density at 1.4 GHz. To test that this was performing as expected, we used a single JVLA data set (JVLA2018, observed in 2018). Two images covering  $18 \text{ arcmin} \times 15 \text{ arcmin}$  were generated using CASA task TCLEAN implementing the MT-MFS (with nterms=2) mode. For one of the images, the reference frequency for the evaluation of the Taylor expansion, which takes into account the frequency dependence of the sky model during deconvolution, was set to 1.4 GHz. Both of these images were primary beam corrected using the WIDEBANDPBCOR task. These were then identically catalogued using PYBDSF with an arbitrary  $8\sigma$  detection threshold (to reduce scatter induced by the fitting routine). As Fig. 3 shows, the median differences between the peak brightnesses and integrated flux densities are 5.2 and 4.7 per cent, respectively. This corresponds

to a median spectral index of  $-0.67$ , which is consistent with the literature (e.g. Condon 1984; Kimball & Ivezić 2008; Smolčić et al. 2017), thus validating this correction method in accounting for the reference frequency differences.

The scatter in the distribution indicates that there is a non-negligible number of sources where this difference can cause 10–20 per cent amplitude adjustments. While this is not sufficient for outright classification using the metric used in this paper,<sup>6</sup> the combination with other factors, such as residual calibration errors, could induce artificial variability in a small number of sources.

Another possible artificial source of variability due to the reference frequency shifting correction could be due to the induced source spectral index caused by differing primary beam attenuation across the bandwidth. The spectral index, used by MT-MFS to rescale the flux densities to 1.4 GHz, would be a linear combination of the source-intrinsic spectral index and a primary beam-induced spectral index, thus causing an incorrect rescaling of the flux densities. The extra primary beam spectral index term,  $\alpha_E$ , can be approximated by<sup>7</sup>

$$\alpha_E = -8 \ln(2) \left( \frac{\theta}{\theta_0} \right)^2 \left( \frac{\nu}{\nu_{\text{ref}}} \right)^2, \quad (3)$$

where  $\theta_0$  is the primary beam full width at half-maximum (FWHM) at the reference frequency,  $\theta$  is the distance from the pointing centre, and  $\nu$  is the observing frequency. Therefore, a flat spectrum source ( $\alpha = 0$ ) located 10 arcmin from the pointing centre would have an additional primary beam-induced spectral index of  $\sim -0.89$ . This would correspond to a shift in flux density of  $\sim 7$  per cent between the frequencies of 1.52 and 1.4 GHz. To solve this, the wide-band primary beam correction, applied with CASA task WIDEBANDPBCOR, models and removes the primary beam-induced spectral index,  $\alpha_E$ .

### 3.4 Absolute flux scaling

Due to the use of the VLA pipeline, a different flux scale was used for the VLA and JVLA data during calibration. However, there is little difference between these flux density scales, and any discrepancies are within the 3–5 per cent error (Perley & Butler 2017). Indeed, the phase calibrator flux densities of all epochs agree fairly well and are all within 5 per cent of each other at 1.4 GHz. These small offsets should be proportional to the source flux density and can therefore be modelled and correction factors derived.

To do this, we use robust linear regression (implemented in the ODR SCIPY Python package) to fit the peak fluxes between each pair of epochs in order to derive single epoch correction factors. Only sources with peak flux densities larger than  $55 \mu\text{Jy beam}^{-1}$  were considered because this corresponds to  $10\sigma$  in the least sensitive epoch (VLA 1996). The more sensitive JVLA 2011 epoch 2 is used as the reference epoch. The scaling factors derived and applied to the peak brightnesses were 1.01, 1.04, and 0.96 for the JVLA 2011 epoch 1, VLA 1996, and JVLA 2018 epochs, respectively.

<sup>6</sup>A 20 per cent flux difference would only give a  $V_s$  (equation 5) of 1.414, assuming a typical 10 per cent error due to calibration and fitting.

<sup>7</sup>See <https://casa.nrao.edu/casadocs/casa-5.6.0/imaging/synthesis-imaging/wide-band-imaging>.

### 3.5 Variability definition

In order to identify variable and transient sources, we adopt the formulation developed by Mooley et al. (2016). We assume that our radio interferometric noise is Gaussian distributed (Condon et al. 1998) and therefore we can compare the flux densities of a source,  $S$ , across two epochs (1,2) with the following equation:

$$\frac{\Delta S}{\sigma} = \frac{S_1 - S_2}{\sqrt{\sigma_1^2 + \sigma_2^2}}, \quad (4)$$

where  $\sigma$  is the measurement error. This comprises the PYBDSF fitting error,<sup>8</sup> the in-band spectral index error ( $< 2$  per cent), and a surface brightness error to quantify slight differences in the  $uv$  coverage, pointing errors, and primary beam correction. We assume a flux density error for the JVLA and VLA data of between 3 and 5 per cent (Morrison et al. 2010; Perley & Butler 2013, 2017). The quantity,  $\Delta S/\sigma$ , is expected to follow the two-sided Student-t distribution and, utilizing the same notation as Mooley et al. (2016), we define the variability t-statistic,  $V_s$ , as

$$V_s = \left| \frac{\Delta S}{\sigma} \right|. \quad (5)$$

The extent of a source's variability between two epochs can be quantified using the 'modulation index',  $m$ , which is defined as

$$m = 2 \frac{S_1 - S_2}{S_1 + S_2} = \frac{\Delta S}{\langle S \rangle}, \quad (6)$$

where  $\langle S \rangle$  is the mean flux density of the source. Due to the expected low number of variable sources, we are more concerned with reliability over completeness. Therefore, we adopt the rather conservative criterion for a variable source, which is identical to that used by Mooley et al. (2016). We define a source as variable if the variable t-statistic,  $V_s$ , is beyond the 95 per cent confidence interval ( $V_s \geq 4.3$ )<sup>9</sup> and its peak brightness changes by  $\geq 30$  per cent (corresponding to  $|m| > 0.26$ ).

### 3.6 Summary

To summarize, the definitions and systematics outlined above lead to the following strategy being adopted in this paper, in order to identify variable and transient sources:

- (i) Each epoch was searched for extended sources and these were identically masked in all epochs.
- (ii) For each epoch, sources were extracted using PYBDSF using an S/N threshold of  $7\sigma$  based upon the false detection and flux recovery tests outlined in Section 3.1. The total number of radio sources considered is around 250–480 due to the differing sensitivities of the epochs.
- (iii) Flux scaling issues due to small errors in the absolute flux scaling and differences in restoring beams are corrected using the routine outlined in Section 3.4.

<sup>8</sup>This error is based upon the Condon (1997) formulation and does not require the Monte Carlo approach used in PYBDSF to evaluate errors as these are only needed for extended sources that are not considered here.

<sup>9</sup>For 2 degrees of freedom, the 95 per cent confidence interval in the Student-t distribution corresponds to a Gaussian probability of more than  $\pm 4\sigma$ . For the Gaussian distribution,  $4\sigma$  corresponds to a probability of about 1/16 000 (0.006 25 per cent). The number of individual measurements in our variability analysis is 3464, which corresponds to 0.2165 false-positive variable sources. See Mooley et al. (2016) and p. 65–67 and table C.8 of Bevington & Robinson (2003) for further details.



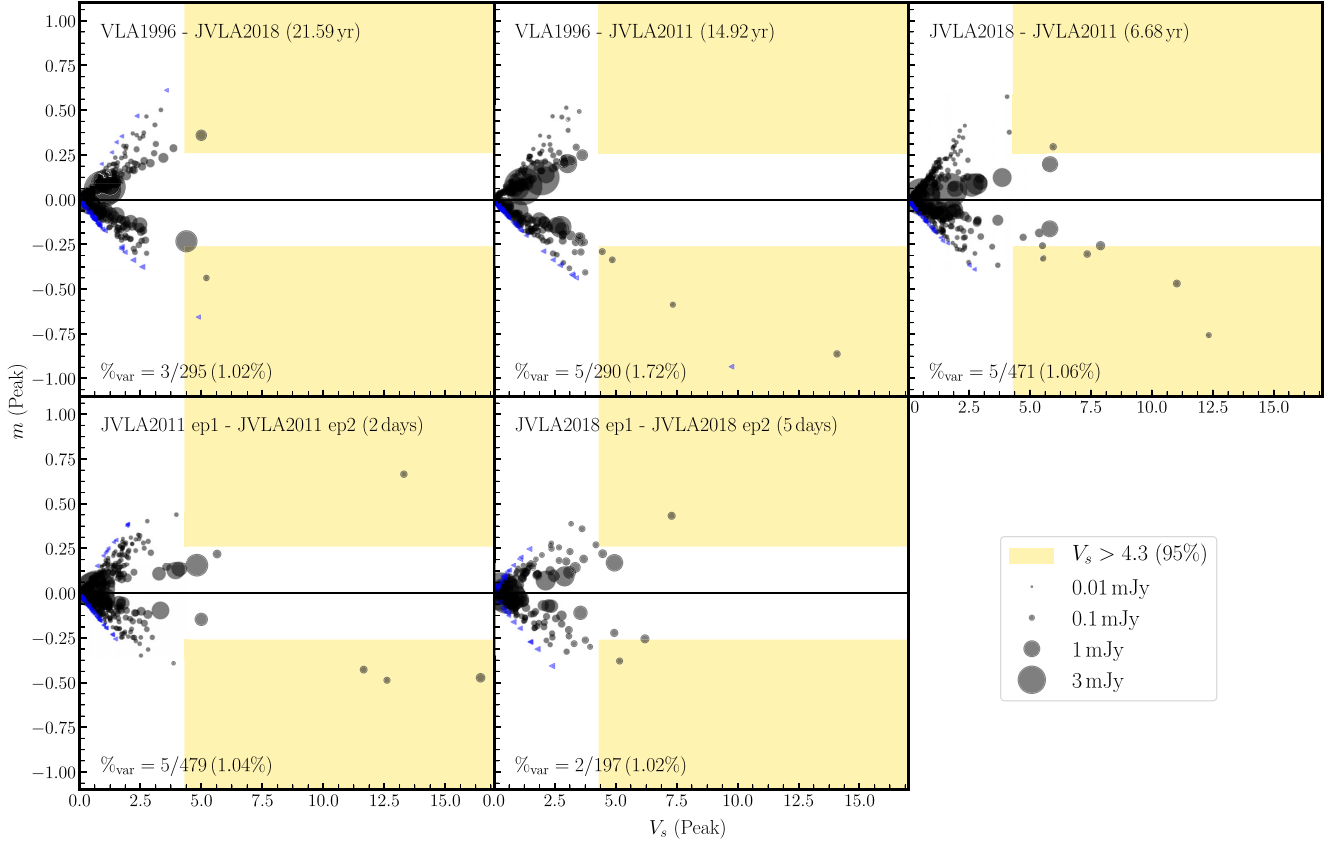


**Figure 4.** The two-epoch comparison comparing the variability statistic  $V_s$  to the modulation index,  $m$ . The black markers correspond to sources that are present in both epochs, while the blue triangles are those sources that have upper limits in one epoch. The marker sizes are proportional to the mean peak brightness,  $\langle S_p \rangle$ . The gold region corresponds to the variability criteria where the variability must be statistically significant, i.e.  $V_s > 4.3$ , and it must have adjusted flux by 30 per cent (i.e.  $|m| > 0.26$ ). The total number of variable sources is higher in this figure as some sources are classed as variables in more than one two-epoch comparison.

(iv) These catalogues were cross-matched and combined using a 1 arcsec search radius. Sources not present in some epochs have upper limits derived, which correspond to  $7 \times$  the local r.m.s.

(v) Using the definitions outlined in Section 3.5,  $V_s$  and  $m$  were derived for all two epoch combinations and variable candidates are identified if  $V_s \geq 4.3$  and  $|m| \geq 0.26$ .

(vi) Sources only present in one of the two epochs being compared have upper limits derived, which correspond to the  $7\sigma$  detection threshold at the source position where  $\sigma$  is derived using the r.m.s. maps generated by PYBDSF. If the detection threshold is smaller than the peak brightness, then  $V_s$  and  $m$  are calculated, using the detection threshold as the peak brightness, otherwise this source is not considered in the two-epoch comparison.

(vii) Next, we separate those sources into transient and variable sources. A source is classed as being variable if the source satisfies the variability criterion and is detected in multiple epochs while a transient source must satisfy the variability criterion but is only detected in a single epoch.

(viii) Finally, variable and transient candidates are checked manually to see if other factors such as nearby calibration errors or poor source-extraction fitting could have artificially induced the variability.

## 4 RESULTS

### 4.1 Variable sources

The aim of this paper is to investigate the long-term  $\mu\text{Jy}$  radio sky. In order to achieve this, we split our JVLA epochs into two sub-epochs separated by short day-week time-scales. This is done to establish whether any long-term variability behaviour is artificially induced by any short-term variability. In light of this, we establish two definitions corresponding to those sources with long- and short-term variability, respectively. The long-term variable candidates are those that satisfy the variability criteria in any two-epoch comparison between the VLA1996, JVLA2011, and JVLA2018 epochs, while the short-term variables are identified as those that satisfy the variability criteria for any two sub-epoch comparisons (i.e. JVLA2011 ep1 and JVLA2011 ep2, JVLA2018 ep1 and JVLA2018 ep2). In Fig. 4, we show the variability index,  $V_s$ , against the modulation index,  $m$ , for all two-epoch and sub-epoch comparisons considered here. Sources that are located in the gold-shaded areas satisfy the variability criteria ( $V_s > 4.3$  and  $|m| > 0.26$ ). The top row corresponds to the long-term variables while the bottom row corresponds to the short-term variables. In total, there are around 479 unique sources being considered in these analyses. The number of sources varies between approximately 200 and 480 due to the differing sensitivities of the epochs.

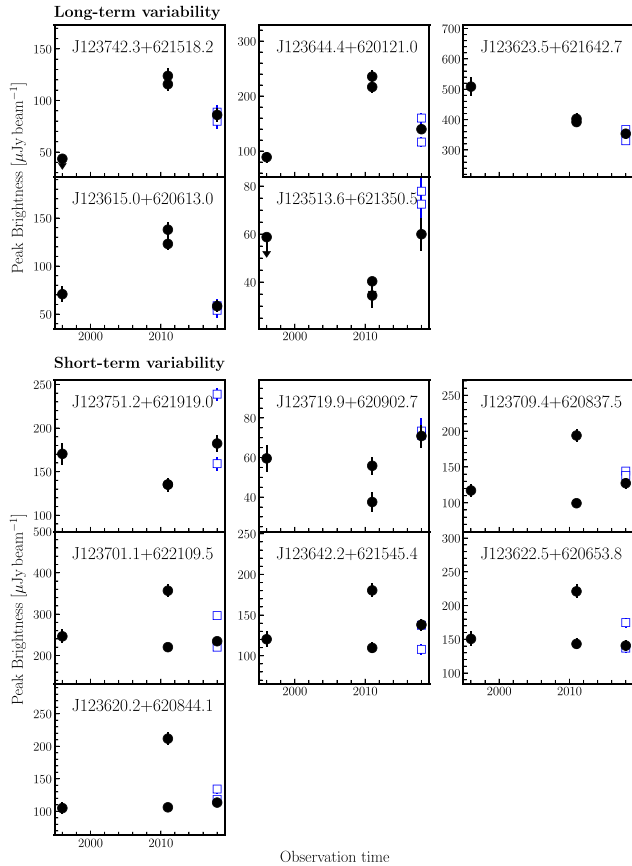


**Figure 5.** Light curves for the variable candidates. The top panel corresponds to those that are classified as long-term variable candidates and the bottom panel corresponds to short-term variable candidates. The entries with asterisks are both long- and short-cadence candidates. The open markers show the combined fluxes for the JVLA epochs illustrating how short-term variability can artificially induce long-cadence variability.

Initial investigations revealed 15 unique variable sources of which 5 were excluded after manual inspection. These were excluded due to a combination of poor source extraction, extended structure, residual calibration errors, and smearing effects. In total, therefore we found 10 unique sources based upon the epoch and sub-epoch comparisons. The epoch-averaged peak flux densities range from 86 to 419  $\mu\text{Jy beam}^{-1}$  with an average flux of 173  $\mu\text{Jy beam}^{-1}$ . The paucity of low-flux density sources  $< 100 \mu\text{Jy beam}^{-1}$  may be indicative of the change in the radio properties of galaxies being primarily driven by AGNs to those driven by star formation processes; however, we note that the variability statistic  $V_s$  is biased towards large S/N, because the fitting error increases with decreasing S/N.

For the candidate long-term variables, around 1–1.8 per cent of the persistent radio sources exhibit significant variability. Note that for the rest of this paper, the term ‘variable fraction’ indicates the percentage of sources that exhibit variability within the total persistent radio population. There is no clear correlation between the cadence time and the variable fraction; however, it is worth noting that the JVLA2018 and JVLA2011 two-epoch comparison is more sensitive ( $\sim 30.5 \mu\text{Jy beam}^{-1}$  detection threshold) hence the number of persistent sources compared differs. If we restrict the JVLA2011 and JVLA2018 epochs to the VLA1996 detection threshold, then we achieve a similar variable fraction of 1.4 per cent.

In total, we find eight sources that are classed as long-term variables. Five of the eight sources are classed as variable on multiple two-epoch comparisons, while two show variability between all epochs.

We classify  $\sim 1$  per cent of our sample as candidate short-term variables, based upon measurements of their flux densities between the JVLA2011 sub-epochs and/or the JVLA2018 sub-epochs. It is worth noting that the JVLA2011 sub-epochs are more sensitive than the JVLA2018 sub-epochs. If we match the JVLA2011 sub-epoch detection threshold to the JVLA2018 sub-epoch detection thresholds, we find a higher variable fraction of  $\sim 2.5$  per cent for the JVLA2011 sub-epochs. In total, we find that seven sources are classed as short-term variables and only one these sources shows variability between both sub-epochs.

Based upon our definitions of long- and short-term variability, we find that 5/10 variable sources are classed as both long- and short-term variables. In these sources, the short-term variability causes the flux to change sufficiently when the sub-epochs are combined such that the sources are also classed as long-term variables. We highlight this effect in the light curves presented in Fig. 5, where the bottom panel shows the influence that the short-term variability has upon the long-term variability measurements. We can partially mitigate this in our sample by isolating those sources identified as long-term variables only. This results in only three sources. However, it is worth stating that the sub-epoch cadence scales sampled here ( $< \text{week}$ ) cannot rule out that the long-term variability in this sample is being induced by  $> \text{week}$  time-scale variability. We would expect the physical mechanism causing variability on short time-scales to be different from the longer time-scales. For example, Ofek et al. (2011) suggest that most short-term variability ( $\sim \text{week}$  time-scales) is extrinsic to the source, while long-term variability could be intrinsic (e.g. quiescent, AGN flaring). Therefore, in order to mitigate this properly and truly separate the physical mechanisms causing variability on different time-scales, we would require multiple epochs that have cadences from day to decade time-scales such that any short-term variability that could induce long-term variability can be identified.

To summarize, we find a total of 10 unique sources exhibiting variability, which corresponds to  $\sim 2$  per cent of the total persistent radio source population comprising 479 sources. Of these 10, we find that 8 are classed as long-term variables while 7 are short-term variables. There are five sources that exhibit both short-term variability and long-term variability for which the flux changes in the short term influence the long-term variability. This leaves three long-term variable candidates; however, it is worth noting that these sources could still be influenced by  $> \text{week}$ -scale variability.

This leads to a few conclusions. First, the 1.4 GHz long-term variable radio sky is relatively sedate, continuing the trend of previous variability surveys with shorter cadences (e.g. Hancock et al. 2016; Mooley et al. 2016). Secondly, at these flux densities, long-cadence variables seem to contain less variable sources than the day-to-week time-scale epochs with the fraction of purely long-term variables being less than 1 per cent of the persistent radio population. However, we note that with the relatively small numbers of variable sources identified in this study, strong statistical conclusions cannot be made.

## 4.2 Transient sources

For the purposes of this paper, we define a transient source as a source that only appears in a single epoch and satisfies the variability criteria (based upon flux density upper limits derived from epochs where the source is not detected). We find no source

that satisfies this criterion. We discuss the implications of this result in Section 5.4. It is worth noting however, that by using this definition, a transient source could simply be a variable source at a flux density below the detection threshold that simply increases in flux during a single epoch.

## 5 DISCUSSION

### 5.1 Comparison to other variability surveys

While this survey does not have the advantage of an ultra-wide field of view, which is advantageous for finding transients and variables (see appendix A of Mooley et al. 2016), it does have the considerable advantage of probing deeper than other surveys across extremely long decadal time-scales. Other surveys at these frequencies suggest that the variable fraction is around 1 per cent or less on minute-to-year time-scales (Croft et al. 2010; Bannister et al. 2011a; Thyagarajan et al. 2011; Mooley et al. 2013). However, deeper surveys suggest that the variable fraction is perhaps higher. Carilli, Ivison & Frail (2003) studied variability in a similar manner to this study using a deep single VLA pointing at 1.4 GHz in the Lockman Hole region. They derived an upper limit of  $\sim 2$  per cent of sources above a detection threshold of  $100 \mu\text{Jy beam}^{-1}$  varying by more than 50 per cent over 19 d and 17 month cadences. This is largely consistent with the results presented here. In our short time-scale study (3 d cadence), we find that no variable sources above  $100 \mu\text{Jy beam}^{-1}$  have a fractional variability  $> 50$  per cent ( $|m| > 0.667$ ).

There is evidence that the number of variable sources detected is a function of sampling cadence. Ofek et al. (2011) carried out a 5 GHz survey across 2.66 square deg of the sky at low Galactic latitudes, which aimed to investigate the variable population on short ( $< \text{day}$ ) time-scales. For sources above flux densities of 1.8 mJy, they found that a high fraction of persistent sources ( $\sim 30$  per cent) were variable at the  $> 4\sigma$  confidence level across day-to-week cadences. This is significantly larger than the results in other surveys, which they attribute to other blind surveys being insensitive to fast variability (e.g. scintillation), caused by averaging across multiple observations. In addition, this survey was conducted at 5 GHz, which has a selection bias towards flat-spectrum radio AGNs. To this end, Ofek et al. (2011) presented a structure function of the variability [defined as  $(S - \langle S \rangle)/\langle S \rangle$ ] that showed that the amount of variability is high on day-to-week time-scales and is constant above around 10 d (albeit with no constraints on longer time-scales). Our results support this, because we find that 70 per cent of our variable sources are variable on the shortest time-scales (days), which could correspond to the high levels of variability suggested by the Ofek et al. (2011) structure function.

Mooley et al. (2016) extended upon this using the 3 GHz CNSS 50 deg<sup>2</sup> pilot survey covering around 3500 radio sources. They find that 2.6 per cent of sources vary on 1.5 yr time-scales, which is considerably more than the weekly (1 per cent) and monthly (0.8 per cent) cadences (which is suggestive that the number of variable sources is a function of time up to the yearly cadences). In total, they find that  $3.8_{-0.9}^{+0.5}$  per cent of sources are variable on time-scales  $< 1.5$  yr. Ignoring the difference in frequency, our results for the shortest time-scales (3 d) are consistent with  $\sim 1.5$  per cent of the sources showing variability.

On the longest time-scales, Hodge et al. (2013) compared the Stripe 82 VLA observation with FIRST and found that  $\sim 6$  per cent of sources in the mJy flux density regime show fractional variability above 30 per cent on 7–22 yr time-scales. This is considerably higher than seen in other studies, which find that the fraction of variables is

of the order of a few per cent or less (Becker et al. 2010; Croft et al. 2010; Bannister et al. 2011b). Our results presented here seem to agree with the latter studies as we find a long-term variable fraction of  $\leq 1$  per cent.

Bannister et al. (2011a) found some evidence that there is a peak in radio variability on time-scales of between 2000 and 3000 d. This was reinforced by Hancock et al. (2016) using a 1.4 GHz study of variability in the Phoenix deep field. Our results suggest that variability reduces in the long decadal cadences and as such implies that the peak in variability suggested by Bannister et al. (2011a) and Hancock et al. (2016) may be viable. However, it is worth noting that this survey is probing a different flux density regime (0.03–2 mJy) to the majority of surveys before (typically  $> 0.5$  mJy). In the standard picture, the radio source population at the flux densities probed by this paper is transitioning from an AGN to a star-forming galaxy-dominated regime, thus the smaller fraction of variable sources may also be an imprint of the change in the nature of the underlying source population.

### 5.2 Sources of variability

To understand the nature of the variability in these sources, we compiled multiwavelength data for each of these sources utilizing the extensive photometry of objects in the GOODS-N field. These data are summarized in Table 2. Redshifts were compiled for the 10 sources from various catalogues (Smail et al. 2004; Wirth et al. 2004; Barger et al. 2008; Skelton et al. 2014; Yang et al. 2014; Momcheva et al. 2016). Of these 12 redshifts, 6/10 are spectroscopic redshifts and the rest are photometric redshifts (of which one is uncertain). The redshifts range from 0.07 to 1.94 with a median redshift of 0.96.

Optical and near-infrared (NIR) *Hubble Space Telescope* (HST) data (Giavalisco et al. 2004; Skelton et al. 2014) plus CFHT  $K_s$ -band imaging (Wang et al. 2010) were used to determine the host galaxy morphologies. For the morphologies, we visually classified the sources into four categories: (1) early-type/bulge dominated, (2) late-type/spiral galaxies, (3) irregular, or (4) unclassified.

The early-type/bulge-dominated group includes those circular/elliptical extended objects whose surface brightness distribution drops towards the edge, while late-type galaxies must have clear spiral features. The irregular category encompasses those with clumpy surface brightness distributions, and sources that are unclassified are those for which a morphology cannot be attained due to being faint. These sources often have undetected low-surface brightness areas, hence they often appear ‘point-like’.

We find that the majority of all variable sources (70 per cent) have early-type morphologies, which are typical of radio-loud AGNs (e.g. Hickox et al. 2009; Griffith & Stern 2010). The remainder comprises two late-type galaxies and one irregular galaxy. To establish whether the radio emission is constrained to the nuclear region, we compared these optical images to the VLA, e-MERLIN (Muxlow et al. in preparation), and VLBI positions (Chi et al. 2013; Radcliffe et al. 2018). Note that the e-MERLIN data form part of the upcoming e-MERGE survey (Muxlow et al. in preparation; Thomson et al. in preparation).

The VLBI observations alone provide the most compelling evidence that the radio emission is caused by an AGN. For extragalactic sources, a VLBI detection implies brightness temperatures in excess of  $10^5$  K, which cannot be reliably attributed to star formation processes alone and must instead be AGN related (Condon 1992; Kewley et al. 2001). We find that 80 per cent (8/10) of the variable candidates exhibit VLBI emission. This includes one source with a  $6\sigma$ – $7\sigma$  VLBI detection coincident with the e-MERLIN



**Table 2.** A summary of the multiwavelength properties and AGN classification for the variable candidates. Long- and short-term variable candidates are denoted by L and S, respectively in the ‘Var. type’ column. Check marks or bold font indicates that the source is classed as an AGN. Redshifts with 68 per cent upper and lower bounds are photometric. The redshift reference abbreviations are as follows: W04 – Wirth et al. (2004), S04 – Smail et al. (2004), B08 – Barger, Cowie & Wang (2008), S14 – Skelton et al. (2014), and Y14 – Yang et al. (2014). The star formation rates (SFRs) were compiled from Whitaker et al. (2014), who used a combination of IR + UV to derive SFRs. The VLBI check marks in brackets correspond to those with  $6\sigma$ – $7\sigma$  VLBI counterparts coincident with the e-MERLIN positions and not reported in Chi, Barthel & Garrett (2013) or Radcliffe et al. (2018). The Donley column corresponds to the IR-AGN classification technique proposed by Donley et al. (2012) and the WISE column corresponds to the Stern et al. (2012) AGN classification technique. The crosses indicate that the sources had the bands necessary to evaluate these metrics but were not classified as an AGN. Entries with hyphens indicate that the measurement could not be taken as the source was out of the field of view of the required bands, while empty entries indicate that the source was not detected in the required bands for classification.

Source ID	Var. type	z	z ref.	Morph.	SFR ( $M_{\odot} \text{ yr}^{-1}$ )	$\langle S_p \rangle$ ( $\mu\text{Jy beam}^{-1}$ )	q24	Donley	WISE	X-rays ( $\text{erg s}^{-1}$ )	VLBI	e-MERLIN
J123742.33+621518.27	L	0.07	B08	2	0.4	103	$0.92 \pm 0.04$	×	–	$2.3 \times 10^{40}$	(✓)	✓
J123623.55+621642.73	L	1.918	S04	1	–	419	<b><math>-1.08 \pm 0.08</math></b>	×	–	–	✓	✓
J123615.02+620613.06	L	$1.2^{+0.10}_{-0.06}$	Y14	1	–	86	–	–	–	–	–	✓
J123751.23+621919.00	LS	$1.11^{+0.03}_{-0.02}$	S14	1	5.6	163	–	×	–	–	✓	✓
J123709.43+620837.55	LS	0.907	W04	1	11.4	134	<b><math>-0.57 \pm 0.14</math></b>	×	–	$3.2 \times 10^{42}$	✓	✓
J123644.48+620121.09	LS	$0.53^{+0.03}_{-0.03}$	Y14	1	–	151	–	–	×	–	–	–
J123622.51+620653.90	LS	$1.94^{+0.12}_{-0.12}$	S14	3	55.0	161.0	<b><math>-0.3 \pm 0.05</math></b>	×	–	–	✓	✓
J123620.27+620844.15	LS	1.016	B08	1	3.5	122	–	×	×	–	✓	✓
J123701.11+622109.55	S	0.8	B08	1	6.2	262	–	×	×	$1.5 \times 10^{42}$	✓	–
J123642.21+621545.42	S	0.858	B08	2	85.7	137	$0.74 \pm 0.04$	×	×	$9.9 \times 10^{42}$	✓	✓

emission, which was not formally reported in Radcliffe et al. (2018) due to their adopted  $7\sigma$  detection threshold. Interestingly, J123642+621545 was measured to have a total flux density of  $343 \mu\text{Jy}$  in the 2004 Global VLBI observations of Chi et al. (2013), almost  $2.5\times$  the VLA flux density. This has subsequently reduced in flux density significantly and was not detected in the 2014 EVN observations of Radcliffe et al. (2018). All of the VLBI positions acquired are consistent with nuclear activity, apart from J123742.33+621518.30 that seems to be offset by around  $0''.24$  from the optical maximum. We discuss this source in Section 5.3.

For the remaining two sources that are not detected by VLBI observations, we use the more sensitive e-MERLIN observations ( $\sim 3 \mu\text{Jy beam}^{-1}$ ; Muxlow et al. in preparation) to search for evidence of nuclear emission in the remaining sources. This resulted in one more source with radio emission coincident with the nuclear regions while the remaining source was out of the field of view of the e-MERLIN observations.

We searched for other indications of AGN activity in these sources in the IR and X-ray bands. Additional *Spitzer* IRAC (3.6–8  $\mu\text{m}$ , Wang et al. 2010; Ashby et al. 2013; Yang et al. 2014) and MIPS (24–70  $\mu\text{m}$ , Dickinson et al. 2003; Magnelli et al. 2011) plus WISE (3–22  $\mu\text{m}$ , Cutri & et al. 2012) photometry was compiled. The X-ray data were derived from the 0.5–7 keV, 2 Ms *Chandra* exposure with the catalogue provided by Xue et al. (2016). A 1 arcsec search radius was used and any counterparts were visually evaluated using the higher resolution radio and optical *HST* images.

These multiwavelength data can be used to further distinguish between AGN or star formation-related emission mechanisms. For the *Spitzer* IRAC NIR bands, we used the IR colour–colour diagnostics of Donley et al. (2012) to establish whether the source had AGN signatures. Here, the presence of a dusty AGN torus causes the spectral energy distribution (SED) to represent a power law in the region between the 1.6  $\mu\text{m}$  stellar bump and the 25–50 K emission from cold dust heated by star formation. The Donley et al. (2012) criterion classifies a source as an AGN if it satisfies all of the following:

$$\begin{aligned}
 x &\geq 0.08 \\
 y &\geq 0.15 \\
 y &\geq (1.21 \times x) - 0.27 \\
 y &\leq (1.21 \times x) + 0.27
 \end{aligned}$$

$$S_{4.5\mu\text{m}} > S_{3.6\mu\text{m}} \wedge S_{5.8\mu\text{m}} > S_{4.5\mu\text{m}} \wedge S_{8.0\mu\text{m}} > S_{5.8\mu\text{m}},$$

where  $x = \log_{10}(S_{5.8\mu\text{m}}/S_{3.6\mu\text{m}})$  and  $y = \log_{10}(S_{8.0\mu\text{m}}/S_{4.5\mu\text{m}})$ . In total, we found that 8/10 sources have NIR counterparts in the four *Spitzer* IRAC bands with S/N ratios larger than  $3\sigma$  in each band. As Fig 6 shows, the majority of these sources show little or no signs of AGN activity in the IR with their NIR characteristics closely following star formation-dominated emission, as shown by the close correlation between the host morphology and the observed NIR colours. For those sources outside of the *Spitzer* IRAC coverage, we cross-matched to the WISE all-sky catalogue (Cutri & et al. 2012), which yielded one additional match. Due to the poor sensitivity in the W3 and W4 bands (only one detection in band 3 and none in band 4), we used the Stern et al. (2012) criterion ( $W1 - W2 \leq 0.8$ ) in order to identify AGNs. Again, this source showed no IR-AGN signatures.

In addition, we use the *Spitzer* MIPS 24  $\mu\text{m}$  flux densities to identify those sources that deviate from the IR-radio correlation. Despite there being some contamination effects (e.g. from high-redshift AGNs, Del Moro et al. 2013), the ratio between the 24  $\mu\text{m}$ ,  $S_{24\mu\text{m}}$ , and 1.4 GHz flux densities,  $S_{1.4\text{GHz}}$  can be used effectively

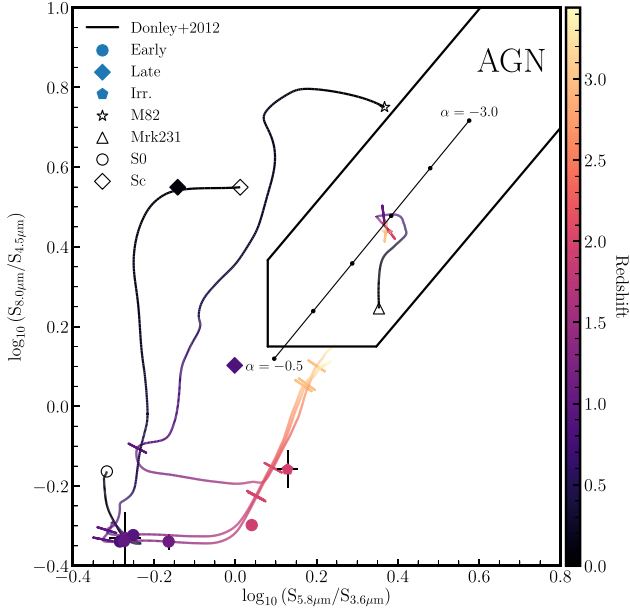


**Figure 6.** *Spitzer* IRAC AGN selection criteria for the variable candidate sample. The solid line corresponds to the revised AGN selection wedge by Donley et al. (2012). The solid line with black markers corresponds to the IR power-law locus in the range  $-3.0 \leq \alpha \leq -0.5$ . Overlaid are the predicted SED colours of the starburst galaxy M82, AGN Mrk231, Sc-type and S0-type galaxies from the SWIRE library (Polletta et al. 2006). The tracks are colour coded across a redshift range of 0–3.4 with the perpendicular bars corresponding to integer redshift intervals. The marker colours of the variable sample correspond to their redshift and are matched to the track colours, while the marker shapes correspond to the host morphology. The AGN-selected objects using these criteria are those in the top right of the figure for all selection methods.

distinguish between AGN and star formation-related activity where systems with an AGN present will produce more radio emission than what is expected from star formation alone (e.g. Appleton et al. 2004; Garn & Alexander 2009; Chi et al. 2013). In addition, this band was chosen to alleviate the effects of confusion that plagues the longer wavelength observations. For each source with 24  $\mu$ m counterparts (5/10), we calculated  $q_{24}$  using

$$q_{24} = \log_{10}(S_{24\mu\text{m}} / \langle S_{1.4\text{GHz}} \rangle). \quad (7)$$

For those sources with 24  $\mu$ m counterparts, we find that three show clear radio-excess signatures from AGN activity ( $q_{24} < 0$ ; Del Moro et al. 2013). We also cross-matched the sample with the 2 Ms *Chandra* X-ray observations presented in Xue et al. (2016). In total, we find that only four sources have X-ray counterparts all of which are classified as an AGN by their selection criteria (see section 2.3.5 of Xue et al. 2016).

In light of this, these commonly used multiwavelength diagnostics are not able to identify all these variable sources as AGN and three sources rely on the identification of a compact radio component. Indeed, based upon the star formation rate (SFR) measurements and IR colours, some of these systems (e.g. J123642.21+621545.42) only show evidence of AGN activity by the existence of a high-brightness temperature core revealed by the VLBI and e-MERLIN observations. This reinforces our belief that high-resolution radio observations are integral to obtaining a full consensus of AGN activity across cosmic time.

In total, we find compelling evidence for AGN activity in 8/10 sources. Of the remaining sources, J123742.33+621518.27 is a possible supernova (see Section 5.3) while J123644.48+620121.08 is outside of the e-MERLIN and VLBI field of view. However, it is worth noting that it is hosted by a typical QSO host, an elliptical galaxy.

Almost all of the variable objects are detected with VLBI, illustrating that there is a milliarcsecond-scale compact radio source producing the variability seen here. Recent VLBI surveys have shown that VLBI-detected sources are becoming more compact at lower flux densities (Deller & Middelberg 2014; Radcliffe et al. 2018). This is supported by semi-empirical simulations that require FR-I-type sources to become core-dominated at low flux densities in order to reconcile the high-frequency ( $> 10$  GHz) number counts with the low-frequency number counts ( $< 5$  GHz) (Whittam et al. 2017). It could be that the variable population at low flux densities traces this population because variable sources will inherently contain a compact radio component. Indeed, the lack of mid-IR AGN signatures (which require a dusty AGN torus to re-radiate UV photons into the mid-IR bands) in any of these objects further adds to this argument, as FR-I galaxies are known to not have dusty tori (e.g. van der Wolk et al. 2010).

For the short-term variable objects, the physical origin of the variability could be scintillation. This has been previously been suggested as the primary cause of most short-term variability at frequencies below 5 GHz. (e.g. Qian et al. 1995; Frail, Waxman & Kulkarni 2000; Ofek et al. 2011). For the long-term variable sample, the source of variability is most likely to be intrinsic to the source and could be caused by changes in the AGN jet power, which has time-scales of years to decades (e.g. Aller et al. 1999; Arshakian et al. 2012), or shocks in the jet (e.g. Woo & Urry 2002; Hovatta et al. 2008). It is worth noting that, without continual monitoring of the source, the origin of the variable emission cannot be distinguished easily. For a sparsely sampled cadence of observations as presented here, the physical processes that cause variability on month-to-year time-scales can masquerade as processes on much longer time-scales. To solve this, more epochs spread over short and long cadences are needed to distinguish between the two.

### 5.3 J123742.33+621518.27 – a possible radio supernova?

This source was noted to be unusual due to the offset between the radio position (provided by e-MERLIN) and optical emission ( $\sim 0''.24$ ) along with low redshift ( $z = 0.07$ ) of the host galaxy. As shown in Fig. 7, the VLA1996 data do not show the compact component that has appeared in the JVA2011 epoch. The peak radio luminosity from the 2012 JVA 5.5 GHz observations of Guidetti et al. (2017) is  $5.67 \times 10^{20} \text{ W Hz}^{-1}$  and the spectral index is  $-0.71$ . This is a typical luminosity for core-collapse radio supernovae, which can range between  $5 \times 10^{19}$  and  $1.3 \times 10^{22} \text{ W Hz}^{-1}$  (Weiler et al. 2002). The  $q_{24}$  radio-excess measure shows no radio-excess emission, which would be indicative of an AGN and there are no signs of AGN activity in the IR diagnostics.

Prior to the emergence of this new compact component, the VLA1996 observations detected diffuse radio emission that was below the formal  $7\sigma$  detection threshold used in this variability study. We hypothesize that this diffuse off-nuclear emission may originate from ongoing star formation processes in the galaxy, hence the diffuse radio-emitting H II region. Low-resolution WSRT imaging (observed in 1999 May; Garrett et al. 2000) recorded an integrated flux density of  $\sim 180 \mu\text{Jy}$ , which is far in excess of the flux densities recorded by the later JVA2011 and 2018

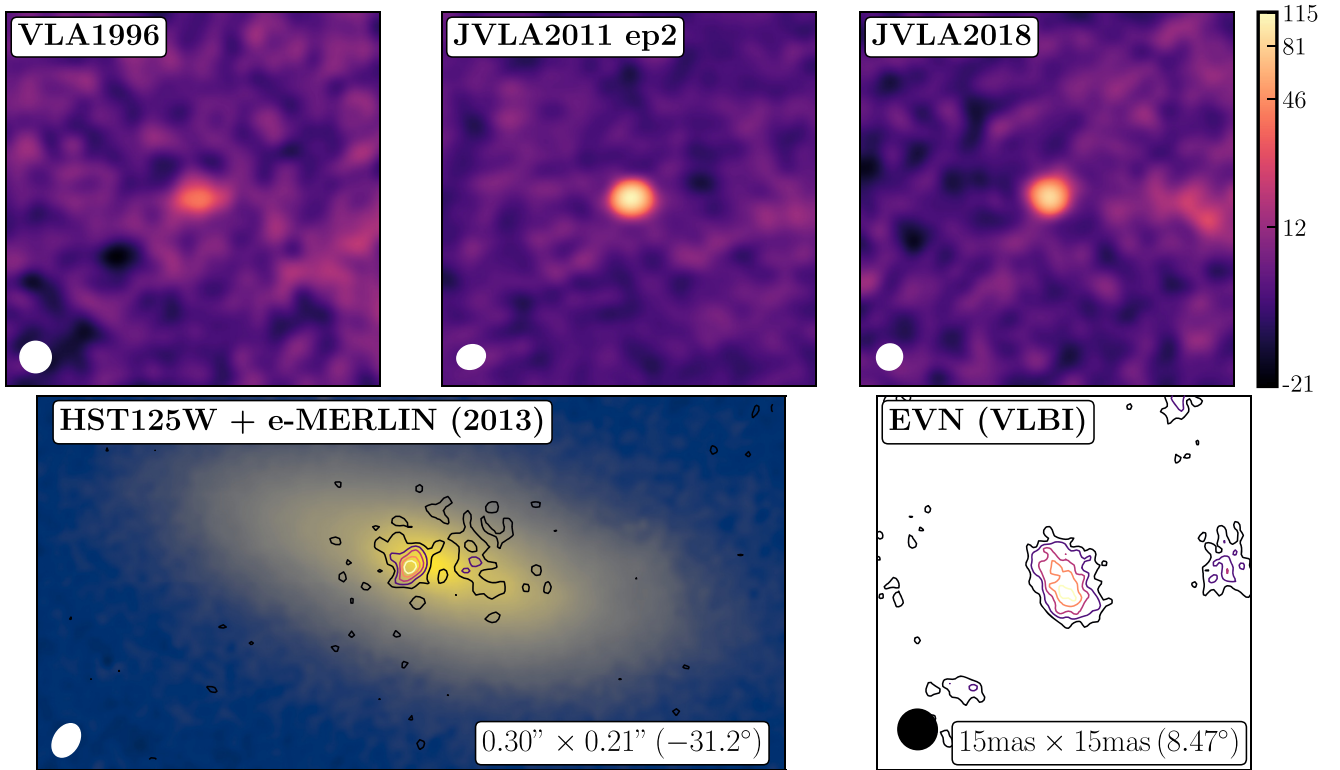


**Figure 7.** Type-II supernovae/LLAGN candidate. The top row shows the evolution of this source from the VLA1996 to the Jvla2018 epochs. The colour scale is identical for each VLA epoch and is in units of  $\mu\text{Jy beam}^{-1}$ . The bottom row illustrates the e-MERLIN offset (Muxlow et al. in preparation) from the astrometry-corrected *HST*125W optical image (Grogan et al. 2011; Koekemoer et al. 2011; Skelton et al. 2014) with the  $6.7\sigma$  VLBI detection in the bottom right panel.

epochs (see Fig. 5). These Jvla epochs show that a new compact radio component dominates over the diffuse emission seen in the VLA1996 epoch. e-MERLIN imaging (observed in 2013; Fig. 7) shows this diffuse emission across the face of the optical host along with an offset compact component. This diffuse emission could be the same star-forming region detected in the VLA1996 data or could be from a low-luminosity AGN jet. The compact source has a  $6.7\sigma$  EVN detection (observed in 2014), which corresponds to an estimated brightness temperature of  $\sim 1.8 \times 10^5$  K. This is slightly larger than expected from star formation processes alone (Condon et al. 1991).

The physical origins of this off-nuclear compact radio source remain unclear but the luminosity, spectral index, and light-curve time-scales are broadly consistent with the characteristics of a powerful core-collapse radio supernova that has occurred between 1996 and 1999, which now dominates the radio emission from the H II region. If this new variable source is a core-collapse radio supernova, it would be the most distant ever discovered.

Unfortunately, with the information available, it is not possible to categorically determine if this off-nuclear variable source is a distant radio supernova or a variable off-nuclear accretion powered source such as one component of a wide-separation binary AGN system. However, this remains an intriguing variable source that will be monitored by future VLBI observations to investigate any expansion of the compact radio emitting region.

#### 5.4 Transient upper limits

In this survey, we detected no transient sources, i.e. those sources that only appear in one epoch alone. Despite the small Field-of-View (FoV) and therefore limiting constraints that this places on the transient fraction we estimated an upper limit to the transient fraction was calculated following the prescription of Ofek et al. (2011). If we assume an arbitrary luminosity function, a uniform density of transient sources in a Euclidean universe, and a primary beam that can be reliably approximated by a Gaussian, then the surface density,  $\kappa$ , of transients brighter than flux density,  $S$ , can be calculated using

$$\kappa(> S) = \kappa_0 (S/S_{\min,0})^{-3/2}, \quad (8)$$

$$\kappa_0 = \frac{3N_b \ln 2}{2\pi r_{\text{HP}}^2} (1 - \exp(-3r_{\text{max}}^2 \ln(2)/2r_{\text{HP}}^2))^{-1}, \quad (9)$$

where  $N_b$  is the number of transients,  $r_{\text{HP}}$  is the primary beam HPBW,  $r_{\text{max}}$  is the maximum radius considered, and  $S_{\min,0}$  is the detection limit at  $r = 0$ , i.e. the primary beam maxima. For the case considered here (no transients), the  $2\sigma$  limit is three events ( $N_b = 3$ , Gehrels 1986). The tightest constraints require the largest number of independent epochs. In this condition, the limiting detection flux density is constrained by the Jvla2018 sub-epochs, which has a central  $7\sigma$  detection limit of  $54.4 \mu\text{Jy beam}^{-1}$ . The primary beam has an  $r_{\text{HP}} = 0.258$  deg and transients were searched to a maximum radius of  $r_{\text{max}} = 0.233$  deg. Substitution into equation (8) and dividing by the number of independent epochs (5) give a  $2\sigma$  upper limit



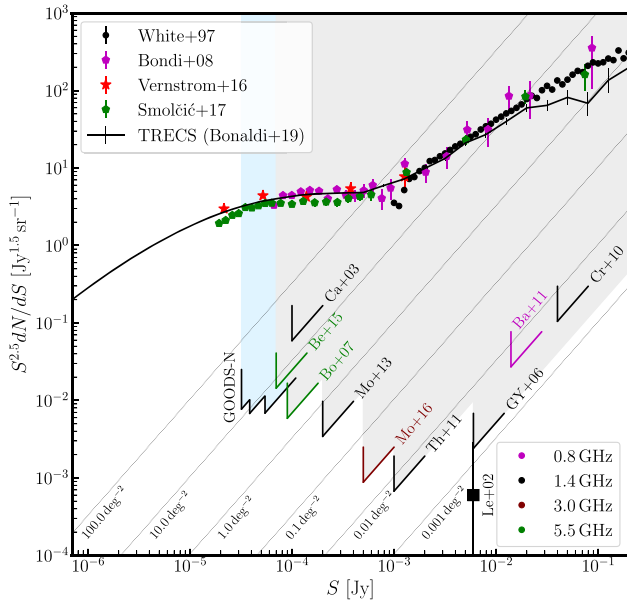


**Figure 8.** The transient normalized areal densities and upper limits with respect to flux density. For a comparison, the normalized differential number counts for persistent sources are overlaid (White et al. 1997; Bondi et al. 2008; Vernstrom et al. 2016; Smolčić et al. 2017). Overplotted are the expected total extragalactic differential number counts from the TRECS simulation (Bonaldi et al. 2019). The wedges correspond to the various 95 per cent upper limits for surveys without transient detection and their colour corresponds to the survey frequency. The shaded area shows the phase space excluded by the current surveys and the abbreviations correspond to the following references: Ca + 03 – Carilli et al. (2003), Bo + 07 – Bower et al. (2007), Be + 15 – Bell et al. (2015), Mo + 13 – Mooley et al. (2013), Mo + 16 – Mooley et al. (2016), GY + 06 – Gal-Yam et al. (2006), Ba + 11 – Bannister et al. (2011a), Cr + 10 – Croft et al. (2010), and Le + 02 – Levinson et al. (2002).

on the areal density  $\kappa(> 54.4 \mu\text{Jy beam}^{-1}) = 5.21 \text{ deg}^{-2}$ . This can be repeated to lower flux densities using different independent epoch combinations. These new constraints are shown Fig. 8, which shows the differential source counts and the limits excluded by previous radio surveys and the results shown here. We have included the differential source counts of persistent sources from observational surveys (White et al. 1997; Bondi et al. 2008; Vernstrom et al. 2016; Smolčić et al. 2017) and the Tiered Radio Extragalactic Continuum Simulation (TRECS; Bonaldi et al. 2019) for comparison. Our results illustrate that there is no upturn in transient events in the  $\mu\text{Jy}$  flux density regime. This is entirely expected; however, it is worth stating here that the majority of these surveys have very different cadence scales, therefore each survey will have a different sensitivity to very short lived transient events. One conclusion that could be made is that there is no significant population below our detection thresholds that are extremely variable on long time-scales. This follows on to the generally accepted paradigm that the  $\mu\text{Jy}$  radio source population becomes increasingly dominated by star-forming galaxies that would not be expected to exhibit strong variability on decadal time-scales.

## 6 CONCLUSIONS

We have conducted a study on the variability in the GOODS-N field using five epochs of the JVLA and VLA data spread across 22 yr. We find a total of 10 variable sources, of which 8 show variability

on long (year–decade) time-scales while 7 show variability on very short (day) time-scales. However, we find that the variability in five of the long-term variables is perhaps influenced by short-term variability, leaving only three sources exhibiting true long-term variability. Nearly all variable sources (9/10) have peak brightnesses above  $100 \mu\text{Jy beam}^{-1}$ , which could be an imprint of transition in the radio populations from AGN to star-forming galaxies at this flux density regime.

Multiwavelength and ultra-high-resolution radio observations reveal that the variability in almost all of these sources can be reliably attributed to AGN activity. The lack of IR-AGN signatures suggests that the variable source population in this regime could be the population of core-dominated FR-I galaxies, without dusty tori, that have been postulated in other wide-field surveys and semi-empirical simulations (Deller & Middelberg 2014; Whittam et al. 2017). The only source without an AGN signature may be a Type-II supernova, which, at  $z = 0.07$ , would make it one of the most distant ever discovered.

In light of this, transient and variable studies are a function of many different parameters such as cadence time, flux density, observing frequency, observing time, and resolution. This paper highlights how important the selection of cadences have upon the interpretation of the final result. In the future, the separation of variability as a function of the aforementioned parameters will require multi-epoch wide-field observations. While such surveys have been conducted at the mJy and Jy regime (e.g. Bower et al. 2010; Croft, Bower & Whysong 2013; Mooley et al. 2016), characterizing the  $\mu\text{Jy}$  regime requires improved snapshot sensitivity and  $uv$  coverage, which will be provided by the next generation of interferometers, such as ASKAP, MeerKAT, SKA, and ngVLA, and their associated transient projects such as VAST (Murphy et al. 2013) and ThunderKAT (Fender et al. 2017).

## ACKNOWLEDGEMENTS

The authors would like to acknowledge the referee Jim Condon and the scientific editor for their useful comments that have greatly helped focus this paper. JFR acknowledges support by the Science and Technologies Facilities Council (STFC), and the Ubbo Emmius Scholarship of the University of Groningen and the South African Radio Astronomy Observatory (SARAO) fellowship that funded this research. APT acknowledges support from STFC grant (ST/P000649/1). The National Radio Astronomy Observatory is a facility of the National Science Foundation operated under cooperative agreement by Associated Universities, Inc. e-MERLIN is a National Facility operated by the University of Manchester at Jodrell Bank Observatory on behalf of STFC. The European VLBI Network (EVN) is a joint facility of independent European, African, Asian, and North American radio astronomy institutes. Scientific results from data presented in this publication are derived from the following EVN project codes: EG078 and GG053. This publication makes use of data products from the Wide-field Infrared Survey Explorer, which is a joint project of the University of California, Los Angeles, and the Jet Propulsion Laboratory/California Institute of Technology, funded by the National Aeronautics and Space Administration.

## REFERENCES

- Aller M. F., Aller H. D., Hughes P. A., Latimer G. E., 1999, *ApJ*, 512, 601  
 Appleton P. N. et al., 2004, *ApJS*, 154, 147

- Arshakian T. G., León-Tavares J., Böttcher M., Torrealba J., Chavushyan V. H., Lister M. L., Ros E., Zensus J. A., 2012, *A&A*, 537, A32
- Ashby M. L. N. et al., 2013, *ApJ*, 769, 80
- Bannister K. W., Murphy T., Gaensler B. M., Hunstead R. W., Chatterjee S., 2011a, *MNRAS*, 412, 634
- Bannister K. W., Murphy T., Gaensler B. M., Hunstead R. W., Chatterjee S., 2011b, *MNRAS*, 418, 2813
- Barger A. J., Cowie L. L., Wang W.-H., 2008, *ApJ*, 689, 687
- Becker R. H., Helfand D. J., White R. L., Proctor D. D., 2010, *AJ*, 140, 157
- Bell M. E., Huynh M. T., Hancock P., Murphy T., Gaensler B. M., Burlon D., Trott C., Bannister K., 2015, *MNRAS*, 450, 4221
- Berger E., Kulkarni S. R., Frail D. A., Soderberg A. M., 2003, *ApJ*, 599, 408
- Bevington P. R., Robinson D. K., 2003, *Data Reduction and Error Analysis for the Physical Sciences*, 3rd edn., McGraw-Hill, New York, NY, USA, Available at: <https://cds.cern.ch/record/1305448>
- Biggs A. D., Ivison R. J., 2006, *MNRAS*, 371, 963
- Bonaldi A., Bonato M., Galluzzi V., Harrison I., Massardi M., Kay S., De Zotti G., Brown M. L., 2019, *MNRAS*, 482, 2
- Bondi M., Ciliegi P., Schinnerer E., Smolčić V., Jahnke K., Carilli C., Zamorani G., 2008, *ApJ*, 681, 1129
- Booth R. S., de Blok W. J. G., Jonas J. L., Fanaroff B., 2009, preprint ([arXiv:0910.2935](https://arxiv.org/abs/0910.2935))
- Bower G. C., Saul D., Bloom J. S., Bolatto A., Filippenko A. V., Foley R. J., Perley D., 2007, *ApJ*, 666, 346
- Bower G. C. et al., 2010, *ApJ*, 725, 1792
- Carilli C. L., Ivison R. J., Frail D. A., 2003, *ApJ*, 590, 192
- Carilli C. L. et al., 2015, preprint ([arXiv:1510.06438](https://arxiv.org/abs/1510.06438))
- Chi S., Barthel P. D., Garrett M. A., 2013, *A&A*, 550, A68
- Condon J. J., 1984, *ApJ*, 287, 461
- Condon J. J., 1992, *ARA&A*, 30, 575
- Condon J. J., 1997, *PASP*, 109, 166
- Condon J. J., Huang Z.-P., Yin Q. F., Thuan T. X., 1991, *ApJ*, 378, 65
- Condon J. J., Cotton W. D., Greisen E. W., Yin Q. F., Perley R. A., Taylor G. B., Broderick J. J., 1998, *AJ*, 115, 1693
- Cornwell T. J., Golap K., Bhatnagar S., 2008, *IEEE J. Sel. Top. Signal Process.*, 2, 647
- Croft S. et al., 2010, *ApJ*, 719, 45
- Croft S., Bower G. C., Whysong D., 2013, *ApJ*, 762, 93
- Cutri R. M. et al., 2012, *VizieR Online Data Cat.*, 2311
- Del Moro A. et al., 2013, *A&A*, 549, A59
- Deller A. T., Middelberg E., 2014, *AJ*, 147, 14
- Dennett-Thorpe J., de Bruyn A. G., 2002, *Nature*, 415, 57
- Dewdney P. E., Hall P. J., Schilizzi R. T., Lazio T. J. L. W., 2009, *Proc. IEEE*, 97, 1482
- sDickinson M., Gialalisco M., GOODS Team, 2003, in Bender R., Renzini A., eds, *Proc. ESO and Universitäts-Sternwarte München, The Mass of Galaxies at Low and High Redshift*. Springer-Verlag, Berlin, p. 324
- Donley J. L. et al., 2012, *ApJ*, 748, 142
- Fender R. et al., 2017, preprint ([arXiv:1711.04132](https://arxiv.org/abs/1711.04132))
- Fong W. et al., 2014, *ApJ*, 780, 118
- Frail D. A., Waxman E., Kulkarni S. R., 2000, *ApJ*, 537, 191
- Gal-Yam A. et al., 2006, *ApJ*, 639, 331
- Garn T., Alexander P., 2009, *MNRAS*, 394, 105
- Garrett M. A., de Bruyn A. G., Giroletti M., Baan W. A., Schilizzi R. T., 2000, *A&A*, 361, L41
- Gehrels N., 1986, *ApJ*, 303, 336
- Gialalisco M. et al., 2004, *ApJ*, 600, L93
- Griffith R. L., Stern D., 2010, *AJ*, 140, 533
- Grogin N. A. et al., 2011, *ApJS*, 197, 35
- Guidetti D. et al., 2017, *MNRAS*, 471, 210
- Hales C. A., 2016, *invgain v1.3*
- Hallinan G. et al., 2017, *Science*, 358, 1579
- Hancock P. J., Drury J. A., Bell M. E., Murphy T., Gaensler B. M., 2016, *MNRAS*, 461, 3314
- Healy F., O'Brien T. J., Beswick R., Avison A., Argo M. K., 2017, *MNRAS*, 469, 3976
- Hickox R. C. et al., 2009, *ApJ*, 696, 891
- Hodge J. A., Becker R. H., White R. L., Richards G. T., 2013, *ApJ*, 769, 125
- Hovatta T., Nieppola E., Tornikoski M., Valtaoja E., Aller M. F., Aller H. D., 2008, *A&A*, 485, 51
- Intema H. T., van der Tol S., Cotton W. D., Cohen A. S., van Bemmell I. M., Röttgering H. J. A., 2009, *A&A*, 501, 1185
- Jauncey D. L., 1968, *ApJ*, 152, 647
- Johnston S. et al., 2008, *Exp. Astron.*, 22, 151
- Kewley L. J., Dopita M. A., Sutherland R. S., Heisler C. A., Trevena J., 2001, *ApJ*, 556, 121
- Kimball A. E., Ivezić Ž., 2008, *AJ*, 136, 684
- Koekemoer A. M. et al., 2011, *ApJS*, 197, 36
- Levinson A., Ofek E. O., Waxman E., Gal-Yam A., 2002, *ApJ*, 576, 923
- Lorimer D. R., Bailes M., McLaughlin M. A., Narkevic D. J., Crawford F., 2007, *Science*, 318, 777
- Lovell J. E. J. et al., 2008, *ApJ*, 689, 108
- McMullin J. P., Waters B., Schiebel D., Young W., Golap K., 2007, in Shaw R. A., Hill F., Bell D. J., eds, *ASP Conf. Ser. Vol. 376, Astronomical Data Analysis Software and Systems XVI*. Astron. Soc. Pac., San Francisco, p. 127
- Magnelli B., Elbaz D., Chary R. R., Dickinson M., Le Borgne D., Frayer D. T., Willmer C. N. A., 2011, *A&A*, 528, A35
- Mohan N., Rafferty D., 2015, *PyBDSF: Python Blob Detection and Source Finder*, Astrophysics Source Code Library, record ascl:1502.007
- Momcheva I. G. et al., 2016, *ApJS*, 225, 27
- Mooley K. P., Frail D. A., Ofek E. O., Miller N. A., Kulkarni S. R., Horesh A., 2013, *ApJ*, 768, 165
- Mooley K. P. et al., 2016, *ApJ*, 818, 105
- Morrison G. E., Owen F. N., Dickinson M., Ivison R. J., Ibar E., 2010, *ApJS*, 188, 178
- Murphy T. et al., 2013, *Publ. Astron. Soc. Aust.*, 30, e006
- Muxlow T. W. B. et al., 2005, *MNRAS*, 358, 1159
- Ofek E. O., Frail D. A., Breslauer B., Kulkarni S. R., Chandra P., Gal-Yam A., Kasliwal M. M., Gehrels N., 2011, *ApJ*, 740, 65
- Offringa A. R., van de Gronde J. J., Roerdink J. B. T. M., 2012, *A&A*, 539, A95
- Offringa A. R. et al., 2014, *MNRAS*, 444, 606
- Oosterloo T., Verheijen M., van Cappellen W., 2010, *Proc. Sci., The Latest on Apertif*. SISSA, Trieste, PoS#43
- Owen F. N., 2018, *ApJS*, 235, 34
- Owen F. N., Morrison G. E., 2008, *AJ*, 136, 1889
- Padovani P., Bonzini M., Kellermann K. I., Miller N., Mainieri V., Tozzi P., 2015, *MNRAS*, 452, 1263
- Perley R. A., Butler B. J., 2013, *ApJS*, 204, 19
- Perley R. A., Butler B. J., 2017, *ApJS*, 230, 7
- Perley R. A., Chandler C. J., Butler B. J., Wrobel J. M., 2011, *ApJ*, 739, L1
- Pietka M., Fender R. P., Keane E. F., 2015, *MNRAS*, 446, 3687
- Planck Collaboration XIII, 2016, *A&A*, 594, A13
- Polletta M. D. C. et al., 2006, *ApJ*, 642, 673
- Qian S. J., Britzen S., Witzel A., Krichbaum T. P., Wegner R., Waltman E., 1995, *A&A*, 295, 47
- Radcliffe J. F. et al., 2018, *A&A*, 619, A48
- Rau U., Cornwell T. J., 2011, *A&A*, 532, A71
- Richards E. A., 2000, *ApJ*, 533, 611
- Skelton R. E. et al., 2014, *ApJS*, 214, 24
- Smail I., Chapman S. C., Blain A. W., Ivison R. J., 2004, *ApJ*, 616, 71
- Smolčić V. et al., 2017, *A&A*, 602, A1
- Stach S. M. et al., 2018, *ApJ*, 860, 161
- Stern D. et al., 2012, *ApJ*, 753, 30
- Thyagarajan N., Helfand D. J., White R. L., Becker R. H., 2011, *ApJ*, 742, 49
- van der Wolk G., Barthel P. D., Peletier R. F., Pel J. W., 2010, *A&A*, 511, A64
- van Haarlem M. P. et al., 2013, *A&A*, 556, A2
- Vernstrom T., Scott D., Wall J. V., Condon J. J., Cotton W. D., Perley R. A., 2016, *MNRAS*, 461, 2879
- Wang W.-H., Cowie L. L., Barger A. J., Keenan R. C., Ting H.-C., 2010, *ApJS*, 187, 251

- Weiler K. W., Panagia N., Montes M. J., Sramek R. A., 2002, *ARA&A*, 40, 387
- Whitaker K. E. et al., 2014, *ApJ*, 795, 104
- White R. L., Becker R. H., Helfand D. J., Gregg M. D., 1997, *ApJ*, 475, 479
- Whittam I. H., Jarvis M. J., Green D. A., Heywood I., Riley J. M., 2017, *MNRAS*, 471, 908
- Williams P. K. G., Bower G. C., Croft S., Keating G. K., Law C. J., Wright M. C. H., 2013, *ApJ*, 762, 85
- Wirth G. D. et al., 2004, *AJ*, 127, 3121

- Woo J.-H., Urry C. M., 2002, *ApJ*, 579, 530
- Xue Y. Q., Luo B., Brandt W. N., Alexander D. M., Bauer F. E., Lehmer B. D., Yang G., 2016, *ApJS*, 224, 15
- Yang G. et al., 2014, *ApJS*, 215, 27

This paper has been typeset from a  $\mathrm{T}_{\mathrm{E}}\mathrm{X}/\mathrm{L}^{\mathrm{A}}\mathrm{T}_{\mathrm{E}}\mathrm{X}$  file prepared by the author.